

# INTERFACE

## **Intimal and medial contributions to the hydraulic resistance of the arterial wall at different pressures: a combined computational and experimental study**

Journal:	<i>Journal of the Royal Society Interface</i>
Manuscript ID	rsif-2016-0234.R1
Article Type:	Research
Date Submitted by the Author:	17-May-2016
Complete List of Authors:	Chooi, Kok Yean; Imperial College London, Bioengineering Comerford, Andrew; Imperial College London, Aeronautics Sherwin, Spencer; Imperial College London, Aeronautics Weinberg, Peter; Imperial College London, Bioengineering
Categories:	Life Sciences - Engineering interface
Subject:	Biomedical engineering < CROSS-DISCIPLINARY SCIENCES, Biomechanics < CROSS-DISCIPLINARY SCIENCES
Keywords:	Permeability, Hydraulic resistance, Constitutive modelling, Intima, Media, Artery

SCHOLARONE™  
Manuscripts

# Intimal and medial contributions to the hydraulic resistance of the arterial wall at different pressures: a combined computational and experimental study

K. Y. Chooi<sup>1,+</sup>, A. Comerford<sup>2,+</sup>, S.J. Sherwin<sup>2</sup>, and P.D. Weinberg<sup>\*1</sup>

<sup>1</sup>Department of Bioengineering, Imperial College London

<sup>2</sup>Department of Aeronautics, Imperial College London

<sup>+</sup>Both authors contributed equally to this work

May 17, 2016

## Abstract

The hydraulic resistances of the intima and media determine water flux and the advection of macromolecules into and across the arterial wall. Despite several experimental and computational studies, however, these transport processes and their dependence on transmural pressure remain incompletely understood. Here we use a combination of experimental and computational methods to ascertain how the hydraulic permeability of the rat abdominal aorta depends on these two layers and how it is affected by structural rearrangement of the media under pressure. *Ex vivo* experiments determined the conductance of the whole wall, the thickness of the media, and the geometry of medial smooth muscle cells and extracellular matrix. Numerical methods were used to compute water flux through the media. Intimal values were obtained by subtraction. A mechanism was identified that modulates pressure-induced changes in medial transport properties: compaction of the extracellular matrix leading to spatial reorganisation of smooth muscle cells. This is summarised in an empirical constitutive law for permeability and volumetric strain. This led to the physiologically interesting observation that, as a consequence of the changes in medial microstructure, the relative contributions of the intima and media to the hydraulic resistance of the wall depend on the applied pressure; medial resistance dominated at pressures above  $\sim 93$ mmHg in this vessel.

Keywords: permeability, hydraulic resistance, constitutive modelling, intima, media, artery

## 1 Introduction

The transport of molecules through the tissues comprising the arterial wall plays an important role in many processes ranging from lipid accumulation in atherosclerosis to contrast agent and drug transport in the diagnosis and treatment of disease. For many of these molecules, the Péclet number (Pe) is substantially greater than one (Baldwin et al., 1997; Hwang et al., 2001) so their transport is dominated by advection - i.e. they are transported by the bulk flow of water. Studies of the anti-proliferative drug paclitaxel have shown the additional complexity that Pe is inhomogeneous through the arterial wall (Creel et al., 2000); understanding such transport requires investigation of the local water transport.

Experimental work on the structural determinants of hydraulic conductance ( $L_p$ ) has focused on *ex vivo* measurements of water flux across segments of arteries (Tedgui and Lever, 1985; Shou et al., 2006). In a few studies, measurements were made before and after selective removal of various wall components, in an attempt to define the causes of the resistance to flow (Weinberg et al., 1997). Interpretation of such experiments is complicated by the collapse of the wall to fill the spaces occupied by the missing components. Measurements have also been made before and after mechanical removal of the endothelium in order to obtain  $L_p$  for the intact and denuded wall and, by subtraction, to estimate  $L_p$  for the endothelium alone. A problem with these methods is that removal of the endothelium may alter properties of underlying layers of the wall by removing a source of vasoactive agents (e.g.

---

\*p.weinberg@imperial.ac.uk

endothelin, a vasoconstrictor whose release is pressure dependent) and by increasing tissue compaction as a result of the artificially elevated water flux.

To overcome limitations inherent in experimental methods, a number of studies have conducted numerical simulations of water flux across the wall. The geometry of the arterial media is commonly idealised as a regular array of cylinders in 2D or 3D, approximating the arrangement of smooth muscle cells (SMCs), embedded in porous medium or fibre matrix simulating the extracellular matrix (Wang and Tarbell, 1995; Huang and Tarbell, 1997; Dabagh et al., 2009b). These models are mathematically elegant. However, detailed microstructural studies have shown that the media comprises fascicles of irregularly shaped SMCs within a highly-structured extracellular matrix (ECM), in which layers of the fibrous proteins elastin and collagen are embedded in a gel-like ground substance consisting of glycosaminoglycans and proteoglycans (Clark and Glagov, 1985). To capture the true anatomy of the media, we recently conducted a combined computational/experimental simulation of water flux in which the medial structure and the permeability of different parts of the ECM were obtained from images of segments of the arterial wall that had been equilibrated with a fluorescent tracer that is restricted to the larger pores through which water flux occurs (Comerford et al., 2015).

When transmural pressure is altered, the medial structure exhibits a non-linear deformation (Holzapfel et al., 2000), with cellular reorganisation as a result of heterogeneous strain fields arising from aligned solid structures. The dependence of permeability on this deformation is a well-known characteristic of the arterial wall but poorly understood. Experimental observations of diameter and  $L_p$  show non-linear relationships with pressure (Baldwin et al., 1997; Shou et al., 2006). Previous studies modelling this dependence (Johnson and Tarbell, 2001; Klanchar and Tarbell, 1987) assumed a relationship between permeability and deformation based on articular cartilage (Mow et al., 1980), and, as above, used an idealisation of the true medial geometry.

In the present study, we have extended and modified our combined computational/experimental approach to study the effects of pressure on water flux across the arterial media, the whole wall and (by subtraction) the intima. Water flux across the whole wall was measured and image-derived data were used to obtain the shape and distribution of smooth muscle cells, and the volume and connectivity of the extracellular space, at a range of pressures; water flux was modelled in these geometries using values for the ECM permeability coefficient ( $k_{ECM}$ ) previously obtained by fibre matrix theory.

## 2 Methods

### 2.1 Overview of the combined computational/experimental approach

Water flux across an *ex vivo* arterial segment of known surface area was measured at a range of pressures, and corresponding values of  $L_p$  for the whole wall were calculated (Figure 1a,b). Albumin labelled with a fluorescent dye that had been added to the working fluid entered the ECM of the wall. Its distribution was mapped by confocal microscopy after  $L_p$  measurements had been completed, following fixation of the tissue at pressure (Figure 1c). The images were overlaid with a structured computational grid and SMCs were removed from the domain using a penalty parameter. This approach provided realistic geometries of the medial layer for numerical modelling; fluid flow was simulated and the intrinsic permeability of small regions within the media was calculated in all directions, using a permeability coefficient for the ECM obtained previously (Figure 1d). Performing these simulations for geometries obtained from tissues exposed to a range of transmural pressures related intrinsic medial permeability to transmural pressure (Figure 1e). Volume fraction change of the medial block within this pressure range was also obtained from the high-resolution images (Figure 1f). Parametric non-linear regression fits of these experimental and numerical data were used to obtain a constitutive relationship between medial permeability and solid volume fraction (Figure 1g). The intimal resistance,  $R_{INT}$ , was determined from wall and medial hydraulic resistances,  $R_{WALL}$  and  $R_{MED}$  (Figure 1h).

### 2.2 *Ex vivo* experiments

#### 2.2.1 Animals

All animal procedures complied with the Animals (Scientific Procedures) Act 1986 and were approved by the Local Ethical Review Panel of Imperial College London. Nine male Sprague Dawley rats ( $266 \pm 6$ g; mean  $\pm$  SEM; Charles River, UK) were housed under a 12h light cycle at 20-25°C. They were fed a normal laboratory diet (LBS Biotechnology Ltd, UK) *ad libitum*.

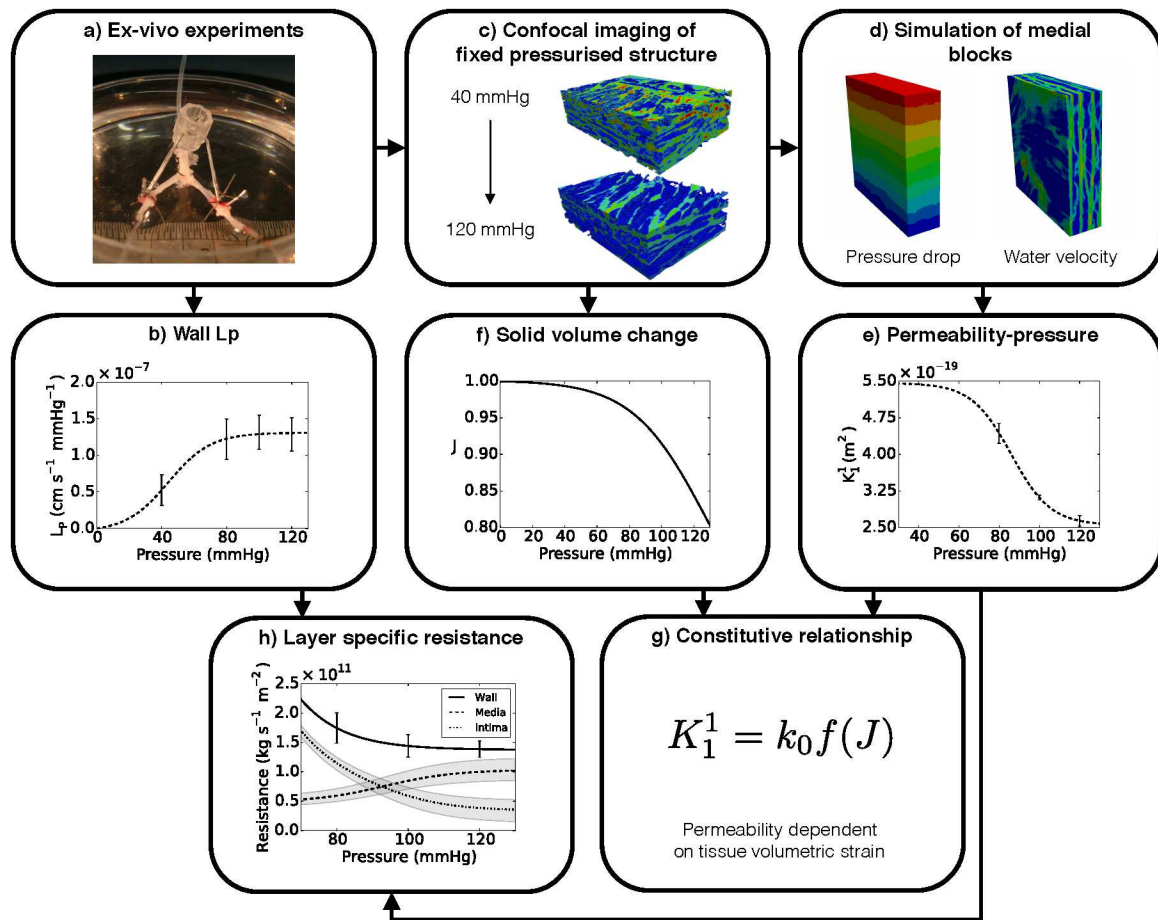


Figure 1: Flowchart of computational/experimental determination of arterial wall transport properties.

### 2.2.2 Vessel isolation

The distal abdominal aorta and proximal iliac arteries were cannulated and removed from animals anaesthetised with isoflurane. This segment is of interest because of its propensity for disease (Mitchell and Schwartz, 1965). Collapse or over-pressurisation of the arteries during the isolation was prevented by a system of reservoirs providing a constant hydrostatic pressure (Tedgui and Lever, 1984; Forster and Weinberg, 1997). Arterial segment lengths and the bifurcation angle were maintained at their *in vivo* values by tying the cannulae to a stereotactic tripod before removal of the vessels from the body. The whole *ex vivo* preparation was placed into a temperature-controlled bath of Tyrode's Salt Solution (TSS; composition in g/l was 8 NaCl, 0.2 KCl, 0.2 CaCl<sub>2</sub>, 0.1 MgCl<sub>2</sub>, 0.05 NaH<sub>2</sub>PO<sub>4</sub>, 1 NaHCO<sub>3</sub>, 1 glucose; pH 6.5) at 37°C that had been pre-equilibrated with 95% air 5% CO<sub>2</sub>.

Figure 2 shows the system used to perfuse the vessel at pressure *ex vivo*. TSS supplemented with 1% rhodamine-labelled bovine serum albumin (Rh-BSA) and 3% unlabelled BSA was introduced into the lumen and the abluminal TSS was replaced with TSS containing 4% unlabelled BSA.

### 2.2.3 Whole wall hydraulic conductance

Steady state  $L_p$  was measured at 4 transmural pressures: 40, 80, 100 and 120 mmHg. Both iliac cannulae were closed to allow measurement of the volume flow rate across the arterial wall by tracking bubble displacement in a graduated tube. The tube was made out of a hydrophobic material in order to prevent bubble slippage (Baldwin et al., 1992). Abluminal fluorescence was monitored over time and steady state transport was observed when fluorescence intensity increased linearly with respect to time; flow rate measurements were then taken for 25 minutes. Each *ex vivo* preparation was exposed to each pressure once, allowing a steady state to be reached each time, with the order of pressures randomised to account for bias arising from time after isolation. Hydrostatic pressure was changed at a rate of 20 mmHg/min.

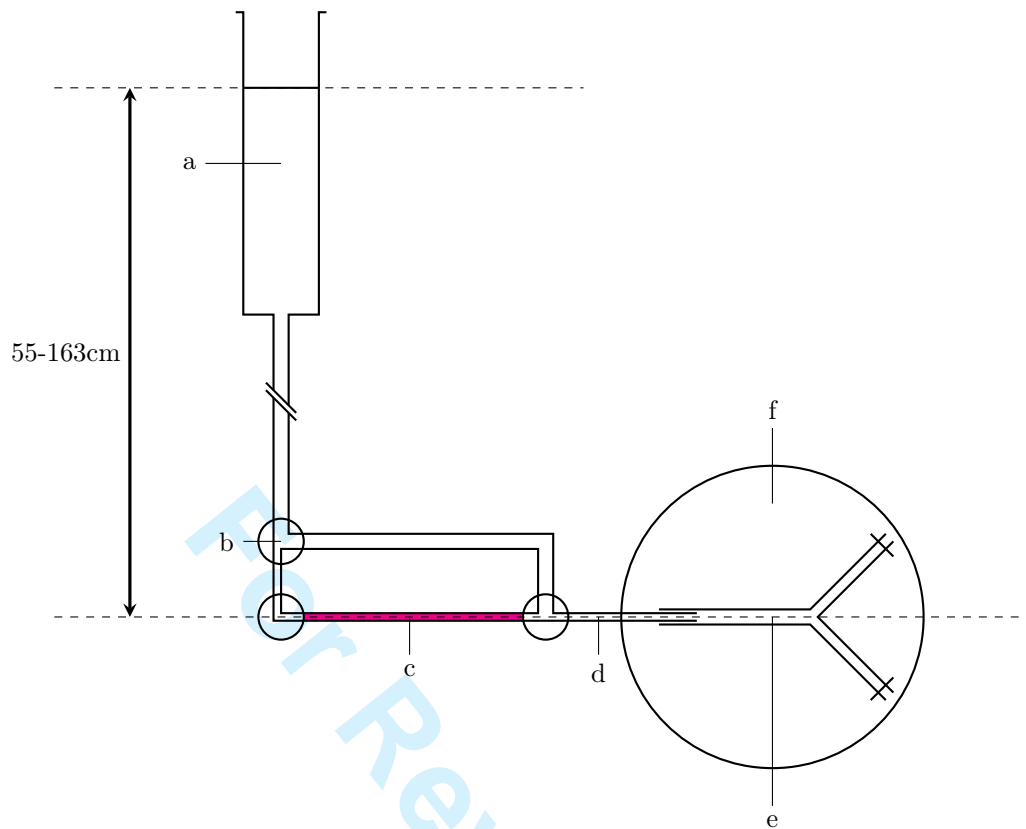


Figure 2: Diagram of *ex vivo* vessel perfusion. (a) TSS reservoir above the vessel, (b) 3-way tap, (c) tracer solution, (d) graduated capillary tube: Inner diameter=  $460\mu\text{m}$ , length=  $30\text{cm}$  (e) isolated aortic bifurcation: Aortic length=  $11 \pm 0.5\text{mm}$ , Iliac length=  $8 \pm 0.5\text{mm}$  (f) temperature-controlled abluminal bath.

The outer surface area,  $A$ , of the bifurcation was determined from measurements of the arterial segment lengths, diameters and branching angles, and  $L_p$  was then calculated:

$$L_p = \frac{\pi \frac{\Delta x_t}{\Delta t} (D)^2}{4A\Delta p}. \quad (1)$$

where  $\Delta x$  is the displacement of the air bubble in time step,  $\Delta t$ , within the graduated capillary of inner diameter,  $D$ .  $\Delta p$  is the transmural pressure across the aortic tissue.

Finally, results were expressed as hydraulic resistance,  $R_{WALL} = 1/L_p$ .

## 2.3 Microscopy and image processing

### 2.3.1 Fixation at pressure and embedding

The aortic bifurcations were fixed and dehydrated whilst maintaining the transmural pressure used for the final  $L_p$  measurement and without removing the vessel from the stereotactic apparatus. The lumen and abluminal surface of the bifurcation were briefly rinsed with TSS and the abluminal bath was replaced with formal sublimate (6%  $\text{HgCl}_2$ , 15% formaldehyde) for 30 minutes. Mercuric chloride acts rapidly (order of seconds) (Baker, 1958) and also prevented elastic recoil of the vessel when it was released from the apparatus. The vessel was post-fixed in 15% formaldehyde overnight, dehydrated with a graded ethanol series (50%, 70%, 90%, 95%, 100%), and embedded in epoxy resin (EPON 812, TAAB) as described previously (Comerford et al., 2015)

### 2.3.2 Confocal microscopy

The lateral walls of vessels fixed at each pressure were imaged in 3D at a position 2mm proximal to the apex of the bifurcation (For full details, see Comerford et al. (2015)). Briefly, embedded arteries were cut in the frontal plane so that the cut face showed a longitudinal section. The cut face was imaged using an inverted laser scanning confocal



microscope (Leica, TCS SP5) with the z-axis of the z-stack aligned perpendicular to the cut face. Rhodamine fluorescence was excited at 575nm; emission was imaged at 585-595nm.

### 2.3.3 Image processing

Five cuboidal blocks (see Figure 3) were extracted from images of three pieces of tissue fixed at each pressure within the physiological range (80, 100 and 120mmHg). Additionally, two blocks were extracted from a single tissue specimen fixed at 40mmHg. Image processing, to correct for intensity attenuation with depth, was performed using Fiji (Schindelin et al., 2012) as described previously (Comerford et al., 2015) but with the addition of three image volume rotations to align the imaging axes to the cylindrical coordinates of the aorta.

## 2.4 Effective permeability

Effective permeability refers to the permeability of a hypothetical, uniform region of tissue that exhibits the same overall fluid mechanical properties as a real region of tissue with a non-uniform microstructure. To determine the effective permeability of a porous medium, the flow field must be determined. Flow around solid objects embedded in a porous matrix is described by Brinkman's equation (see Wang and Tarbell (1995); Huang and Tarbell (1997); Comerford et al. (2015)). In the arterial media the solid objects are the SMCs<sup>1</sup> and the surrounding medium is the porous ECM. In the present study, the ECM was assigned an isotropic permeability based on previous models of porous media, which have been validated against experimental data (Kim and Tarbell, 1994; Ethier, 1991); the chosen value,  $k_{ECM} = 1.32 \times 10^{-18} \text{ m}^2$ , represents a mean of the reported values. The same value was used at all applied pressures for two reasons: (i) the changes in the volume of the ECM were small, and (ii) the partitioning of water between different compartments of the ECM is complex and it is possible that applied stresses could increase, decrease or not affect the hydration of the part of the ECM through which the majority of water transport occurs. (For example, although increasing the transmural pressure reduced ECM volume, it might have moved water from the relatively impermeable fibrous protein compartment to the more permeable glycosaminoglycan component). The value of  $k_{ECM}$  was also increased and decreased by 20% in the analysis to cover variations reported in literature. Note that the blocks of tissue on which we base our numerical simulations are highly anisotropic - e.g. the SMC are not arranged isotropically and therefore neither is the ECM - and this anisotropy is captured and included in the model. It is the *microscopic* anisotropy of the ECM is not captured, and which we therefore ignore.

We recently outlined a new approach to determine the effective permeability of the arterial media (Comerford et al., 2015) in the open-source spectral/hp element code Nektar++ (Cantwell et al., 2015). Briefly, in this approach we first determine the flow around SMCs in a representative region of the realistic microstructure obtained from confocal imaging data (Figure 1c and 3(a)). In this method the SMCs are not segmented; rather, the imaging data are directly incorporated into the simulation and regions corresponding to the SMCs are allocated a high resistance. Flow simulations are performed in each of the main directions of the arterial wall (radial, axial and circumferential directions) by applying a pressure drop. From these simulations we can determine mean volumetric velocity ( $\langle \mathbf{u} \rangle$ ) and pressure gradients ( $\langle \nabla p \rangle$ ) Using Darcy's law:

$$\langle \mathbf{u} \rangle = \frac{\mathbf{k}}{\nu} \langle \nabla p \rangle, \quad (2)$$

where  $\nu$  is the kinematic viscosity and  $\mathbf{k}$  is the permeability tensor,

$$\mathbf{k} = \begin{bmatrix} k_{rr} & k_{rz} & k_{r\theta} \\ k_{rz} & k_{zz} & k_{z\theta} \\ k_{r\theta} & k_{z\theta} & k_{\theta\theta} \end{bmatrix}, \quad (3)$$

we can form an over-determined system of equations that can be solved using a least squares approach to find the components of  $\mathbf{k}$ . This tensor can be diagonalised to find the principal components of fluid transport of the arterial wall ( $K_1^1$  is the approximate radial component - it deviates on average by  $3.4^\circ$  from the radial axis - and  $K_1^2$  and  $K_1^3$  are the two transverse components). Figure 3 illustrates the concept of effective permeability in the arterial wall.

<sup>1</sup>Shanahan et al. (1999) showed that a SMC immersed in a solution that is hypertonic by 100 mOsm (equivalent to a pressure of -1930 mmHg) will lose 8% of its volume in 5 seconds. Using a typical SMC length, diameter and volume from Todd et al. (1983), and for simplicity assuming a cylindrical geometry and that the cell membrane has a much higher resistance to water flux than the cytoplasm, we compute  $L_p = 2 \times 10^{-10} \text{ cm/s mmHg}$  for a cell. If the whole wall ( $\sim 5$  laminae thick) were composed of cells, it would have  $L_p = 10^{-11} \text{ cm/s mmHg}$ . That is many orders of magnitude lower than the  $L_p$  observed for the whole wall in the present study, and hence it is a reasonable simplification to assume that the cells are impermeable.

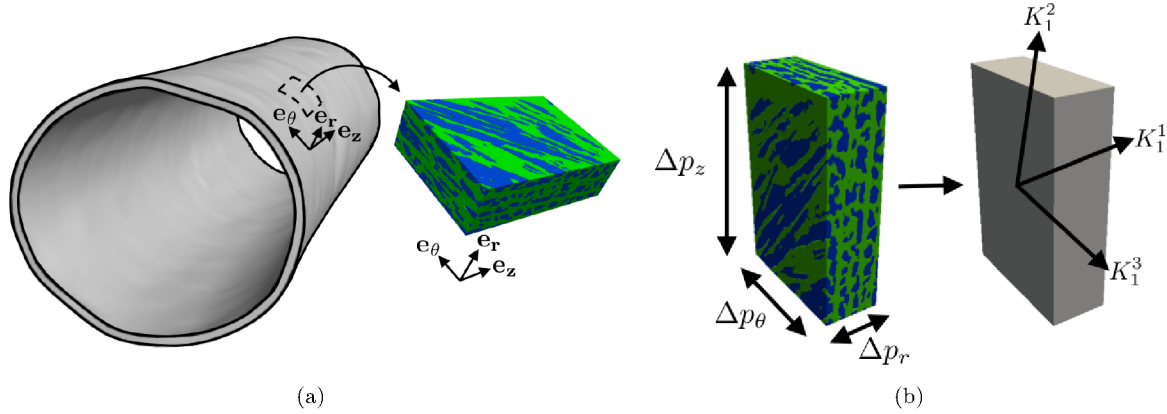


Figure 3: (a) Representation of a block of medial tissue and the orientation when it is extracted from the arterial wall. (b) Simulation of flow in the realistic medial microstructure (left) due to three coordinate-aligned pressure drops can be reduced to three principal measures of permeability (illustrated on the right):  $K_1^1$ ,  $K_1^2$  and  $K_1^3$ .

A difference between our previous and present studies is that in the previous one the local concentration of fluorescent tracer was used to estimate the local porosity of the ECM, as well as to identify SMCs, whereas in the present study it was only used to identify SMCs. That change was necessary because no transmural pressure gradient was applied in the earlier experiments and hence tracer concentrations could reach an equilibrium; equilibration was prevented by the application of pressure in the present study, meaning that the local tracer concentration could reflect transport gradients as well as variation in porosity. The images of fluorescence could still be used to identify SMC as these completely exclude the tracer. The ECM in which the SMC were embedded was assumed to have a uniform porosity.

The above method to calculate the permeability was utilised for 17 tissue blocks (to cover the pressure range: 40, 80, 100 and 120mmHg). For each block, three simulations were performed to extract velocity and pressure data in each of the coordinate directions.

## 2.5 Porous media mixture theory

Hydrated soft biological tissue, such as the arterial wall, can be treated as a mixture of fluid and solid constituents. In the arterial wall the solid constituents represent the SMC and structural molecules (e.g. proteoglycans, collagen and elastin) and the fluid is water. In Figure 3 blue regions represent the impermeable SMCs and the green region is the porous ECM where water flows.

Deformation of soft biological tissue leads to interstitial fluid transport, which can be summarised by the biphasic theory of Mow et al. (1980). A small volume ( $dV$ ) of porous medium comprises a volume of solid ( $dV^S$ ) and volume of fluid ( $dV^F$ ). This allows us to define the volume fraction ( $\phi^S$ ,  $\phi^F$ ) of the two components:

$$\phi^S = \frac{dV^S}{dV}, \quad \phi^F = \frac{dV^F}{dV}. \quad (4)$$

For a saturated mixture these fractions must obey the saturation condition (Holmes and Mow, 1990):

$$\phi^S + \phi^F = 1. \quad (5)$$

As both the solid and fluid are intrinsically incompressible we can write:

$$\phi_R^S = J\phi^S, \quad (6)$$

where  $\phi_R^S$  is the volume fraction in the reference state (0mmHg configuration) and  $J$  is the volumetric ratio between the deformed and reference configurations. ( $J = \det \mathbf{F}$ , where the tensor  $\mathbf{F} = \partial \mathbf{x} / \partial \mathbf{X}$  is the deformation gradient that maps material points ( $\mathbf{X}$ ) in the reference configuration to the deformed configuration ( $\mathbf{x}$ ) - see Spencer (1980)). Volume change is due to fluid entering or leaving a region of tissue.

Several permeability constitutive relationships have been proposed for articular cartilage under deformation (see e.g. Holmes and Mow (1990); Ateshian et al. (1997); Ateshian and Weiss (2010)). Following Ateshian and Weiss

(2010), we write the constitutive relationship for the permeability ( $\mathbf{K}$ ) in the material configuration as:

$$\mathbf{K} = \sum_{a=1}^3 K_1^a \mathbf{M}_a, \quad (7)$$

where  $\mathbf{M}_a = \mathbf{A}_a \otimes \mathbf{A}_a$  ( $\mathbf{A}_a$  representing the unit normal vectors to three planes of symmetry in the tissue) restricts the permeability to three orthogonal planes of symmetry in the arterial wall - radial (a=1) and two transverse planes (a=2,3) - and  $K_1^a$  is a function of the relative volume change ( $J$ ), given by:

$$K_1^a = k_0 f(J), \quad (8)$$

where  $k_0$  is the permeability at 0mmHg and  $f(J)$  describes how the permeability changes with pressure-driven deformation. (In the arterial wall the circumferential and axial permeability will also depend on the orientation of the SMCs.) Equation 8 is a constitutive relationship that describes the dependence of the intrinsic tissue permeability as a function of deformation, thus characterising the effect of local volume changes on hydraulic permeability.  $k_0$  and  $f(J)$  can be determined using our method in section 2.4 for tissue pressurised at different lumen pressures.

## 2.6 Solid volume fraction

### 2.6.1 SMC volume fraction

The confocal data were transformed onto the quadrature points of the computational mesh (64000 mesh elements,  $8 \times 10^6$  quadrature points). Thresholding fluorescence intensities divided the volume into two compartments, the volume occupied by the smooth muscle cells ( $V^{SMC}$ ) and the remaining volume, corresponding to the ECM. The volume fraction of the SMCs ( $\phi^{SMC}$ ) and ECM ( $\phi^{ECM}$ ) of a medial block with volume  $V$  can then be defined by:

$$\phi^{SMC} = \frac{V^{SMC}}{V} \text{ and } \phi^{ECM} = 1 - \phi^{SMC}. \quad (9)$$

To investigate errors in thresholding and their significance, two observers independently chose thresholds for 5 images each. They were found on average to be within 3% of each other, and this led to a 2% difference in the measured volume fraction of the SMCs

### 2.6.2 Mobile water in the ECM

To determine the mobile water content of the ECM<sup>2</sup>, experiments were conducted in which porcine aortic tissue was compressed. The tissue samples (n=4, area: 100 mm<sup>2</sup>) were weighed before and during compression between two porous platforms at a pressure of 100mmHg in a humidified chamber until the compressed tissue mass was constant. Loss in mass was due to loss of water, interpreted as the mobile water. The mobile water content was 37.5% of the initial wet weight.

### 2.6.3 Solid volume fraction

The solid volume fraction is the solid matrix (e.g. structural ECM fibres, solid components of cells) and water that is not transported e.g. water bound to proteoglycans or inside cells. From our experiments, the mobile water fraction ( $\phi^W$ ) for the whole block of tissue is 0.375. The mobile water content of the ECM in the reference state is given by:

$$\phi_R^{W,ECM} = \frac{\phi^W}{\phi_R^{ECM}}. \quad (10)$$

From equation 10 we can define a solid volume fraction that varies with pressure:

$$\phi^S = \phi^{SMC} + \phi^{ECM}(1 - \phi_R^{W,ECM}). \quad (11)$$

Pore closure is intrinsically included in the value of  $\phi^{SMC}$ , derived from the confocal data at each pressure, since an expansion of the fraction occupied by SMC would correspond to a reduction in the fraction occupied by ECM, and vice versa. Equation 11 was evaluated for each pressure (40, 80, 100 and 120mmHg) and the change in volume fraction of the solid constituents in the wall - ( $J$  in equation 6) - was determined.

<sup>2</sup>extrafibrillar extracellular water



## 2.6.4 Radial compression

To provide an estimate of radial compression, the average ECM compression between SMCs and the average SMC thickness within the medial blocks were determined. In this approach, the sum of the distances between SMCs in the radial direction was determined in a 1D measurement across the total block thickness for transmural pressures of 80 and 120mmHg. The percentage change in ECM thickness was then determined from these two measurements. A similar approach was used to determine the mean SMC radial width: the total thickness in the radial direction of SMCs was determined and divided by the number of SMC layers.

## 2.7 Intimal hydraulic resistance

Using our combined computational/experimental approach it is possible to determine the mean  $L_p$  of the intima. The arterial wall can be envisaged as an electrical resistor network, where the intimal and medial layers provide resistances in series to water flow that add to give the overall wall resistance,  $R_{WALL}$  (The adventitia is ignored as it provides little resistance to transport).  $R_{WALL}$  was obtained from the *ex vivo* experiments described in section 2.2.3. This value represents the wall resistance for the entire bifurcation, therefore the following analysis must also be performed over this region. For the medial layer, the permeability can be reformulated as a medial resistance ( $R_{MED}$ ) based on thickness ( $T$ ) data from the confocal images and the viscosity of water ( $\mu$ ):

$$R_{MED} = \frac{\mu T}{K_1^1}. \quad (12)$$

The thickness is an average of the mean medial thickness in the abdominal aorta and iliac arteries ( $T = 36.7\mu\text{m}$ ). This mean was weighted to account for the different surface areas of the iliac and aortic portions of the bifurcation:  $53.8\pm 2\%$  and  $46.2\pm 2\%$  of the total area, respectively. The  $K_1^1$  value is the radial permeability component for the blocks extracted from the abdominal aorta. From our data, the iliac arteries exhibit some differences to the abdominal aorta e.g. some breakup of the elastin sheets; however, the overall structure of the SMCs is similar, which is the main influence on radial permeability. For example, at 80 mmHg the structure had a volume fraction of  $32\pm 3\%$ , which is similar to the equivalent value for the abdominal aorta of  $34\pm 1\%$ . Finally, using these results,  $R_{INT}$  can be expressed as:

$$R_{INT} = R_{WALL} - R_{MED}. \quad (13)$$

## 3 Results

### 3.1 Hydraulic conductance of the whole wall

Using the methods described in section 2.2.3, we measured  $L_p$  as a function of pressure. A sigmoidal function was fitted to the data using parametric non-linear regression (Figure 4). This function was evaluated against a linear fit using the corrected Akaike information criterion ( $AIC_c$ ) (Hurvich and Tsai, 1989). The sigmoidal fit had a lower  $AIC_c$  than the linear.

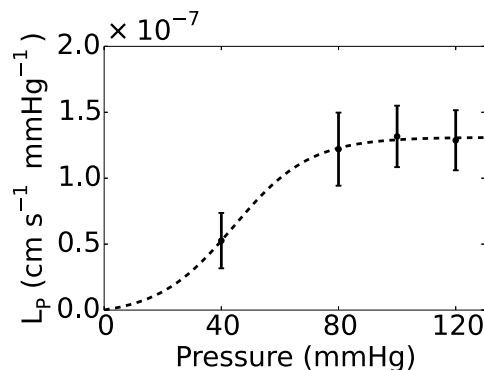


Figure 4:  $L_p$  for the whole wall as a function of transmural pressure difference. Data are represented as mean  $\pm$  SEM (n=7-8)

### 3.2 Permeability of the media

The results for permeability versus pressure obtained from the numerical simulations are shown in Figure 5 for the three principal components. The first principal component can be considered the radial component (see “Principal vectors of the permeability tensor - alignment” in Supplementary material), whilst the transverse directions are not the cylindrical or axial coordinates of the artery wall since SMCs are not perfectly aligned with these directions; transport occurs preferentially along the direction of SMC orientation. This is in line with our previous observations that orientation of SMCs alternates through the thickness of the media (Comerford et al., 2015).

The dotted line was determined by parametric non-linear regression; the fit was only performed in the data range. A sigmoidal function was evaluated against different models (quadratic and cubic polynomials), having a different number of parameters, using the  $AIC_c$ . In all cases the sigmoidal function had the lowest  $AIC_c$ , and is therefore the preferred model for these data.

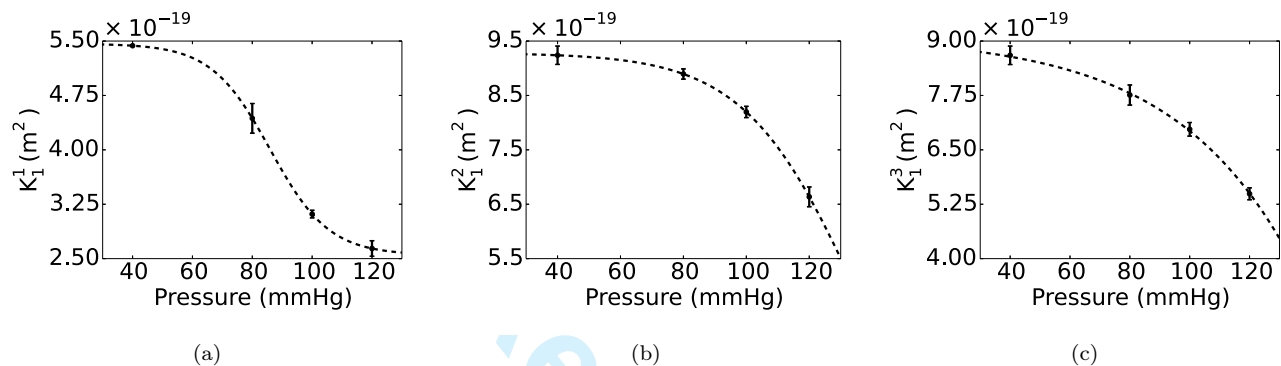


Figure 5: Permeability-pressure relationship in the principal axes of the arterial wall: (a) radial component,  $K_1^1$  (b) transverse component,  $K_1^2$  (c) transverse component,  $K_1^3$ .

### 3.3 Solid volume fraction of the media

The solid volume fraction of the media is shown in Figure 6(a). As above, it was fitted to a sigmoidal function, enabling the reference solid fraction ( $\phi_R^S = 0.63$ ) to be determined. The increase in solid volume fraction with pressure is due to compression of the ECM, which drives water out. This can be expressed in terms of the relative volume change (Equation 6) from the zero pressure state, shown in Figure 6(b). Between 80 and 120mmHg, the percentage volume change is  $14 \pm 1\%$  and the ECM compression in the radial direction (obtained by the methods described in section 2.6) was  $\sim 5\%$  across the entire medial block.

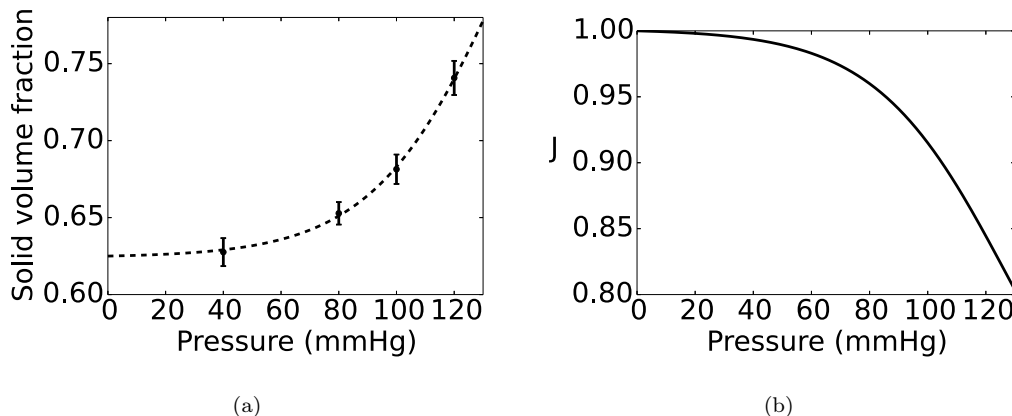


Figure 6: Structural deformation of medial soft tissue due to arterial pressurisation: (a) medial layer solid volume fraction; (b) volumetric change of solid constituents in the media ( $J$ )

### 3.4 Constitutive relationship

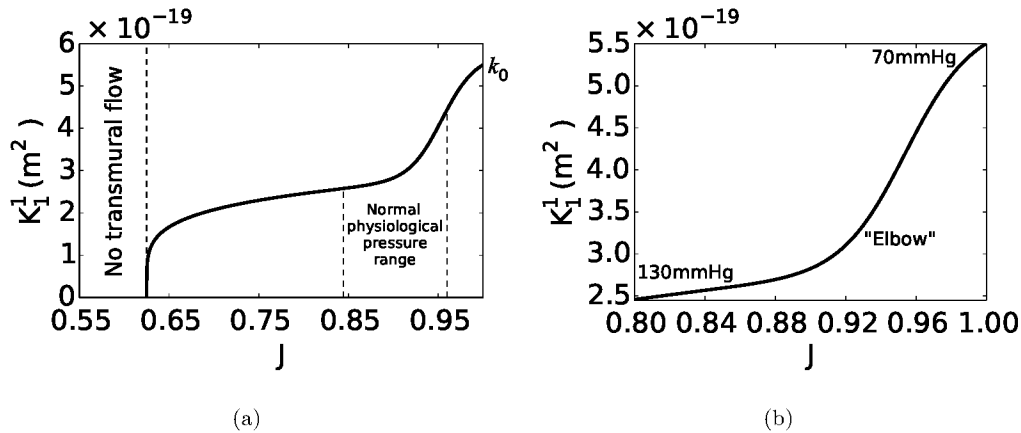


Figure 7: Relationship between radial permeability ( $K_1^1$ ) and volumetric change of solid constituents in the media ( $J$ ). (a) is the full range and (b) is zoomed in on the region corresponding to a pressure range of 70-130mmHg. The “elbow” represents the region where the gradient of  $K_1^1$  transitions from a steep to a more gradual reduction with pressurisation.

For the constitutive relationship we focus purely on the radial direction, since transverse pressure gradients in the wall are small compared to those in the radial direction. The relationship, shown in Figure 7, is described by the following equation:

$$K_1^1 = k_0 \left( \frac{1 - \phi^S}{1 - \phi_R^S} \right)^m \left[ p_1 + \frac{p_2}{1 + e^{(J - p_3)p_4}} \right]. \quad (14)$$

The unknown parameters were determined by parametric nonlinear regression of the permeability and volume change data to be:  $p_1 = 0.52, p_2 = 0.52, p_3 = 0.95$  and  $p_4 = 55.12$ .  $k_0 = 5.51$  is a product of the fit. Equation 14 can be separated into three distinct parts: the permeability in the reference state ( $k_0$ ); a conservation constraint,  $\left( \frac{1 - \phi^S}{1 - \phi_R^S} \right)^m$  with  $m = 0.2^3$ ; and the physical behaviour derived from our computational/experimental approach,  $p_1 + p_2 / (1 + e^{(J - p_3)p_4})$ . The conservation constraint is a high-pressure physical constraint: when the pores that hold water are fully closed ( $J = \phi_R^S$ ), no transmural flow occurs. This would occur only at pressures well beyond the physiological range. The permeability in the physiological range is shown in Figure 7(b). Further details about the constitutive relationship and its finite element implementation in the open-source software FEBio (Maas et al., 2012) are given in appendix A.

### 3.5 Mean intimal hydraulic resistance

$R_{INT}$  was calculated using equation 13, where  $R_{WALL}$  was calculated from the experimental total wall  $L_p$  data and  $R_{MED}$  from equation 12.  $R_{INT} < R_{MED}$  for pressures above  $\sim 93$ mmHg (Figure 8). In this study the medial thickness was based on an average thickness for the abdominal aorta and iliac arteries. The measured mean medial thickness was  $36.7 \mu\text{m}$ . An average across all pressures was used as the change in medial thickness with pressure is small - e.g. less than  $4 \mu\text{m}$  in the aorta between 80mmHg and 120mmHg. The band on  $R_{MED}$  and  $R_{INT}$  represents the effect of allowing the assumed ECM permeability to change by  $\pm 20\%$ .

## 4 Discussion

In our *ex vivo* experiments, the hydraulic conductance of the whole wall more than doubled as the transmural pressure difference increased from 40 to 80mmHg but then remained constant in the 80-120mmHg physiological range (Figure 4). (Note that  $L_p$  is defined as the flow per mmHg pressure gradient, and that it accounts for changes in surface area but not wall thickness; if it remained constant as pressure increased from 80 to 120mmHg that

<sup>3</sup>The choice of  $m$  is arbitrary - it describes how the curve transitions to zero when all water has been exuded

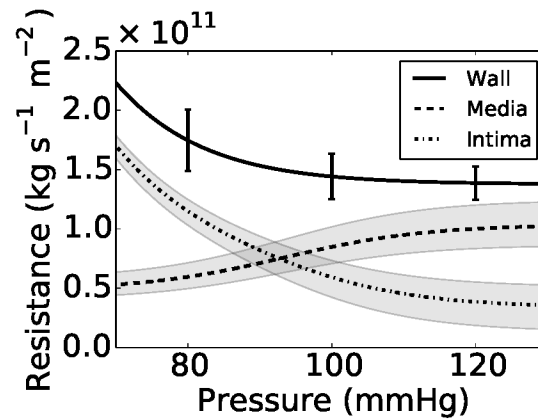


Figure 8: Decomposition of  $R_{WALL}$  for a 2-layered structure. The error bars are SEMs ( $n=7-8$ ). The grey band around the medial resistance represents a  $\pm 20\%$  change in the permeability of the ECM - to cover the range of values reported in literature. The grey band around the intimal resistance represents the propagation of this uncertainty.

would mean that the flow per unit surface area of the wall increased 50%.) The dependence of aortic  $L_p$  on pressure has varied between previous studies: like us, Baldwin et al. (1992); Baldwin and Wilson (1993); Shou et al. (2006) obtained a plateau over the physiological range, but Tedgui and Lever (1984) found a substantial decrease in  $L_p$  as pressure increased; Baldwin and Wilson (1993); Shou et al. (2006) showed a decrease in  $L_p$  from sub-physiological to physiological pressure whereas Baldwin et al. (1992) found  $L_p$  was constant over this range. (And at 100 mmHg - the centre of the physiological range - the study of Shou et al. (2006) gave an  $L_p$  approximately five-fold higher than the one obtained here, presumably reflecting their use of the rat thoracic aorta rather than the thinner terminal aorta and proximal iliac arteries.)

This variation may reflect the complexity of the physical interaction between pressure and wall thickness. Increased pressure will distend the vessel and thus will tend to reduce wall thickness. The extent of the distension will depend on the material properties of the wall; the thoracic aorta used in the four studies listed above is likely to be more elastic than the abdominal segment used here. The reduction in the wall thickness will also be affected by any changes in hydration that result from the distension. Wall thickness will also be affected by solvent drag, but the direction is hard to predict. Considering flow through a compressible sponge, analogous to the wall tissue, the sponge will be stretched by solvent drag if it is anchored at its upstream surface but will be compacted if it is anchored at its downstream surface. Because of the concentric layering of more and less distensible components in the wall, the actual response of the aorta to increased transmural flow is not intuitively obvious. Net effects of all these factors, and of endothelium-derived vasoactive agents, on wall thickness have been measured: Baldwin et al. (1992) found a decrease in wall thickness as pressure was increased from 50 to 100mmHg, but no further change when pressure was increased to 150mmHg.

Medial permeability was computed using microstructures obtained from confocal images of tissue fixed at different pressures: mapping the uptake of a fluorescent extracellular fluid-phase marker in three dimensions allowed separation of the tissue into SMC and ECM compartments with sub-micron spatial resolution, avoiding the assumptions of idealised medial architectures in earlier work. The simulations required no free parameters and only one value from the literature: the average permeability of the ECM. Several values have been reported (Dabagh et al., 2009a; Wang and Tarbell, 1995; Huang and Tarbell, 1997), so it is possible that the actual ECM permeability differs slightly from the chosen value. The shape of the  $K_1^1$  versus pressure curve would not alter if the value were changed, but the absolute magnitude would. The former was confirmed by increasing and decreasing the value of  $k_{ECM}$  by 20%. The calculated medial resistance consistently lay below the experimentally measured total wall resistance at all pressures, so the magnitudes are at least plausible.

The simulations showed that  $K$  in all three principal axes decreases substantially as pressure is increased within the physiological range. Variability between simulations based on different samples obtained at the same pressure was small, and the changes with pressure were large, supporting the view that the trends with pressure are reliable. Deformation of the arterial wall under increased pressure causes a reduction in  $K_1^1$  through ECM compaction. This compaction, resulting from pore closure, was evident visually in the confocal data and confirmed by computing  $\phi^S$  and  $J$ : as pressure increased from 80 to 120mmHg, the volume reduction of the ECM was  $14 \pm 1\%$ . Radial compression of the ECM, obtained by the method described in section 2.6, was  $\sim 5\%$  over the same pressure range.

1  
2 The SMCs, which can be considered nearly incompressible, are brought into closer proximity to one another due to  
3 ECM compaction. Additionally, the cells become thinner due to stretching. Between 80 and 120mmHg, the mean  
4 number of SMCs per block in the radial direction increased from 3.47 to 4.34 and the mean cell width decreased  
5 from 2.11 to 1.83 $\mu\text{m}$ . This further increases the resistance to paracellular water transport.

6 These observations are captured in our proposed constitutive relationship, which for the first time relates radial  
7 permeability to strain driven by ECM compaction (Figure 7). The relationship between the permeability of soft  
8 biological tissues and volume change (or volumetric strain) is well known in the realm of articular cartilage and  
9 ligament mechanics (Ateshian and Weiss, 2010; Holmes and Mow, 1990; Ateshian et al., 1997; Weiss and Maakestad,  
10 2006). In the present study narrowing of intercellular channels accounts for more than  $\sim 80\%$  of the permeability  
11 change within the physiological range, justifying our assumption that the ECM permeability is constant with  
12 pressure. Note that the “elbow” in Figure 7(b) is not an artefact arising from the fitting of a sigmoidal function to  
13 the permeability data (Figure 5(a)) - it arises from a similar kink in the relation between pressure and the change in  
14 solid volume (Figure 6(a)). Our results differ from previous models and assumptions (Simon et al., 1998; Klanchar  
15 and Tarbell, 1987; Johnson and Tarbell, 2001) presumably because we derived our deformation relationship from  
16 experimental data and took into account image-derived aspects of the medial microstructure.

17 Our image-based numerical simulations also demonstrated that medial permeability varies with direction, and  
18 that this anisotropy is pressure dependent. At 80mmHg the permeability in the transverse direction was 2 times  
19 larger than in the radial direction; at 100mmHg this ratio increased to 2.6 but at 120mmHg it reduced to 2.5,  
20 suggesting that additional pressurisation might further reduce anisotropy. *In vivo*, the largest pressure gradient  
21 occurs from the luminal to the abluminal side. Transverse components are significantly smaller, but they can rise  
22 in areas where geometrical undulations and uneven wall deformation occur.

23 The directionally varying trend can be explained as follows: ECM compaction causes  $K_1^1$  to reduce at a lower  
24 pressure than  $K_1^{2,3}$  due to intercellular channels narrowing preferentially in the radial direction. In the transverse  
25 directions the tissue stiffens preferentially along principal directions related to the orientation of collagen (Holzapfel  
26 and Ogden, 2010); collagen and SMCs have similar orientations in the arterial media (Holzapfel et al., 2002).  
27 Combined, these effects mean that the relative ease of water transport in the transverse directions is elevated due  
28 SMC alignment; however radial transport will always dominate in the arterial wall due to the transmural pressure  
29 gradient.

30 A number of experiments have attempted to determine endothelial  $L_p$  by comparing measurements of water  
31 flux obtained before and after removal of the endothelial layer (Tedgui and Lever, 1984, 1985). As already noted,  
32 the unstated assumption that  $L_p$  for the rest of the wall is unchanged by this procedure may be incorrect since a  
33 source of vasoconstrictors and vasodilators has been removed and because solvent drag is increased. An alternative  
34 approach has been to investigate  $L_p$  of endothelial monolayers cultured on porous substrates *in vitro* (Cancel and  
35 Tarbell, 2010, 2011). The drawback of this method is that the artificial environment may degrade the barrier  
36 properties of the endothelium. It is known that these monolayers have elevated permeability to small proteins such  
37 as albumin, which, like water, are transported through intercellular junctions.

38 In the present study, the combination of experimental and numerical techniques gave  $L_p$  for the whole wall  
39 and for the media. Hence  $L_p$  for the intima could be obtained by subtraction; intimal, medial and total wall  
40 resistances are obtained from fully intact tissue with this method. The implicit assumption that all the adventitia  
41 was removed when the vessel was cleaned is unlikely to be critical because the adventitia has a loose structure that  
42 is not expected to offer much resistance to water flux. The results presented in Figure 8 demonstrate that the  
43 intima provides the largest contribution to  $R_{WALL}$  below  $\sim 93$  mmHg whilst the medial layer dominates above  $\sim 93$   
44 mmHg<sup>4</sup>. At 80mmHg the medial layer represents  $\sim 40\%$  of the  $R_{WALL}$ , while at 120mmHg it represents  $\sim 80\%$ .  
45 (Shou et al. (2006) obtained approximately 50% for all pressures from 80 to 120 mmHg). This dominance will likely  
46 increase for thicker walled arteries, in which the media contributes a higher percentage of the wall thickness. Intimal  
47 resistance appeared to decrease with pressure. We hypothesise that this results from pressure induced stretch of  
48 the endothelium, and the resulting shortening of the intercellular junctions. Stretch of the endothelium is known  
49 to increase permeability to albumin (Fry, 1973).

50 The methods applied in this study could be used to quantify other transport properties of tissue, such as diffusiv-  
51 ity. Recent work by Levin et al. (2004) showed for various drugs and macromolecules that transmural and transverse  
52 diffusivities in segments of the calf carotid artery were significantly different. Using our computational/experimental  
53 approach we could characterise anisotropy of drug/macromolecule diffusion in more specific locations (e.g. at sites  
54 prone to, or protected from, disease), and understand how microstructural reorganisation affects diffusivity.

55 The methods have a number of limitations. First, arteries *in vivo* are exposed to pulsatile pressures but both

56  
57  
58 <sup>4</sup> The crossover point has an uncertainty based on the  $\pm 20\%$  ECM permeability. In the present study the range was from 86 - 101  
59 mmHg



our experimental and numerical studies used steady pressures. It is unclear how cyclical pressure changes would affect the microstructure of the wall. Second, we have treated the ECM as a homogenous medium whereas it is actually composed of different compartments of differing resistance to water flow and - potentially - different levels of water loss under applied pressure. Third, for practical reasons, the computation of the medial permeability was limited to blocks taken from the left and right side of the abdominal aorta. Ideally, blocks would be sampled over many different tissue regions e.g. in the iliac arteries and the inner and outer walls of the abdominal bifurcation. Unfortunately, from a computational perspective this is still challenging, given the need for repeated sampling and three simulations to determine the permeability tensor (in this study the total number of core hours totalled 73440 for the 17 tissue blocks). Furthermore, to have sufficient accuracy in the experimental measurements, the hydraulic conductance in this study had to be measured over a sufficiently large area of artery. As advances are made in experimental methods, smaller more localised tissue regions will be considered.

## Author contributions

K.Y.C and A.C contributed equally to this study and manuscript. K.Y.C developed and performed the experiments, computations and analysis. A.C developed and performed computations and analysis. P.D.W advised on the experimental design and provided feedback and suggestions on the manuscript. S.J.S provided advice on the spectral/hp element method.

## Funding Statement

This study was funded by Imperial College's British Heart Foundation Centre of Research Excellence (RE08/002/23906), a British Heart Foundation programme grant (RG11/5/28743) and a Marie Curie fellowship (Project reference: 294104).

## A Finite element implementation of the medial layer permeability constitutive relationship

This section shows how the developed constitutive relationship can be implemented in the open-source finite element software, FEBio (Maas et al., 2012). Medial permeability as a function of volumetric deformation is given by

$$k_1^a = k_0 \left( \frac{1 - \phi^S}{1 - \phi_R^S} \right)^m \left[ p_1 + \frac{p_2}{1 + e^{(p_3 - J)p_4}} \right]. \quad (15)$$

Direction	$p_1$	$p_2$	$p_3$	$p_4$	$k_0^*$	$m^*$
$K_1^1$	0.52	0.52	0.95	55.12	5.51	0.2
$K_1^2$	0.36	0.68	0.82	15.29	9.29	0.2
$K_1^3$	0.63	0.39	0.90	27.20	8.43	0.2

Table 1: Material coefficients for different directions in the arterial wall. \*not material parameters

Following the method of Ateshian and Weiss (2010), to evaluate the permeability in a nonlinear finite element formulation, the permeability must be linearised and thus the rate of change of permeability with deformation must be evaluated. If we assume that the tissue in the material frame is governed by

$$\mathbf{K} = \sum_{a=1}^3 K_1^a \mathbf{M}_a, \quad (16)$$

then the rate of change of permeability in the material frame is given by

$$\dot{\mathbf{K}} = 2 \frac{\partial \mathbf{K}}{\partial \mathbf{C}} = \sum_{a=1}^3 \mathbf{K}_1^a \otimes \mathbf{M}_a. \quad (17)$$

$\mathbf{K}_1^a$  can be expressed in the spatial frame as

$$\hat{\mathbf{k}}_1^a = J^{-1} \mathbf{F} \hat{\mathbf{K}}_1^a \mathbf{F}^T = 2J^{-1} \left[ I_3 \frac{\partial K_1^a}{\partial I_3} \mathbf{I} \right], \quad (18)$$

where  $I_3 = J^2$  and  $\mathbf{I}$  is the identity matrix. Substituting equation 15 into equation 18, gives:

$$\hat{\mathbf{k}}_1^a = \frac{k_0}{J^2} \left( \frac{1 - \phi^S}{1 - \phi_R^S} \right)^m \left[ \left( p_1 + \frac{p_2}{1 + e^{(p_3 - J)p_4}} \right) \left( \frac{m\phi_R^S}{J - \phi_R^S} - 1 \right) + \frac{Jp_2p_4 e^{(p_3 - J)p_4}}{(e^{(p_3 - J)p_4} + 1)^2} \right]. \quad (19)$$

To demonstrate how medial compression relates to water flux, a cuboidal region ( $50 \times 80 \times 80 \mu\text{m}$  in the radial, axial and circumferential directions, respectively) was created and discretised using PreView ([www.febio.org](http://www.febio.org)). A biphasic analysis was then undertaken in FEBio (Maas et al., 2012). For this analysis, the medial tissue consisted of a solid matrix (neo-Hookean material,  $E=0.1$  kPa and  $\nu=0.4$ ) and a permeating fluid with a hydraulic permeability governed by equation 19. The tissue was compressed in the radial direction by fixing one end and applying a fluid pressure to the other. The fixed bottom surface was allowed to drain freely, whilst all other surfaces were impermeable. The lateral walls were fixed, except for the radial displacement, to restrict compression to the radial direction. The applied pressure gave a maximum radial displacement of 4.6% in the physiological range. A summary of boundary conditions is given in Figure 9(a). Figure 9(b) shows the flux of water in the block at a location approximately  $10 \mu\text{m}$  from the fixed surface as the tissue is compressed. The shape of the flux curve is indicative of the permeability constitutive relationship: initially the permeability is higher which with application of pressure causes the flux to increase. As the fluid is exuded the permeability reduces and does not drop rapidly with volume. This is seen by a reduced gradient of fluid flux.

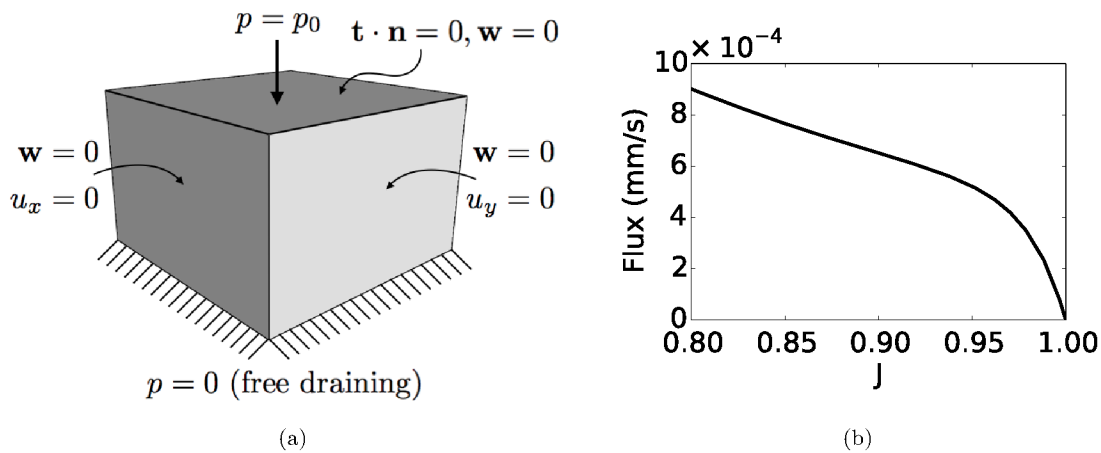


Figure 9: (a) Boundary conditions for the biphasic analysis.  $\mathbf{w}$  is the water flux,  $p$  is the pressure,  $\mathbf{t}$  is the traction vector,  $\mathbf{n}$  is the normal vector and  $u$  the displacement. (b) Water flux variation with volume as the medial tissue is compressed. Data extracted from an element approximately  $10 \mu\text{m}$  from the fixed surface.

## Supplementary Information

### Principal vectors of the permeability tensor - alignment

For the radial direction, which is well defined (being perpendicular to the endothelium), the results are consistent - directions do not change with pressure (Table 2). The other two principal directions, which are less well defined, are consistent within a floating frame of reference - i.e. within each block the numbers are highly consistent.

Table 2: Absolute angle between principal permeability directions and the cylindrical coordinates of the arterial wall

	Block	Radial direction	Axial direction*	Circumferential direction*
80 mmHg	1	2.6°	19.1°	19.1°
	2	4.4°	19.8°	20.3°
	3	2.6°	17.9°	18°
	4	4.4°	10.7°	10.7°
	5	2.6°	2.0°	2.8°
100 mmHg	6	2.6°	31.2°	31.1°
	7	2.6°	50.2°	50.2°
	8	2.6°	8.5°	8.6°
	9	2.6°	15.9°	16.6°
	10	4.8°	1.4°	2.0°
120 mmHg	11	4.4°	29.8°	29.4°
	12	3.6°	59.0°	58.9°
	13	2.6°	5.2°	5.3°
	14	3.6°	7.0°	7.0°
	15	5.1°	22.6°	22.1°

\*Alignment in the transverse plane of the wall has no fixed reference as the confocal images may be rotated; hence it cannot be easily interpreted

### Fixation of tissue in deformed state

In order to obtain realistic images of wall structure in vessels subjected to physiologically relevant transmural pressures, it was necessary to obtain fixation of all the elastic components of the wall while still in the stressed configuration. Otherwise, elastic recoil once the pressure is removed would have introduced artefacts into the images e.g: wavy or wrinkled elastic lamellae in the tunica media. Elastin is difficult to fix with common aldehyde fixation (Fung and Sobin, 1981), retaining its elasticity even after prolonged fixation in a deformed state. A comparison of common fixatives was conducted to select a suitable one. Formal sublimate (FS) was prepared by making a saturated solution of  $\text{HgCl}_2$  in 15% formaldehyde. As the elasticity of elastin is attributed to hydrophobic interactions of its component amino acids, dehydration in the strained state was also trialled with each fixative.

The original length ( $l_o$ ), length during fixation ( $l_d$ ) and final length after fixation and dehydration ( $l_a$ ) of each sample were recorded and the results expressed as percentage of strain retained after fixation and dehydration ie:

Percentage of strain fixed =  $\frac{l_a - l_o}{l_d - l_o}$ . Results are shown in Figure 10.

### Sample bubble displacement data

Bubble speeds were recorded in the range ( $0.46\text{mm min}^{-1}$ ,  $3.25\text{mm min}^{-1}$ ) at 40mmHg and 120mmHg respectively (Figure 11).

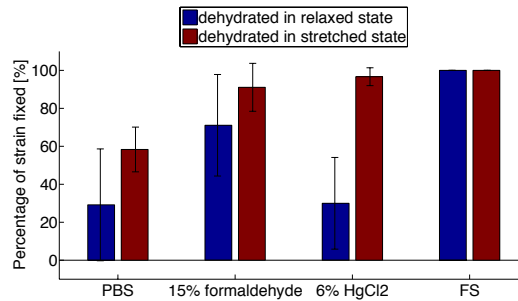


Figure 10: Results of fixation and dehydration trials: dehydration of stretched samples resulted in less recoil for all fixatives. FS performed best of all the fixatives, preserving 100% of the strain.

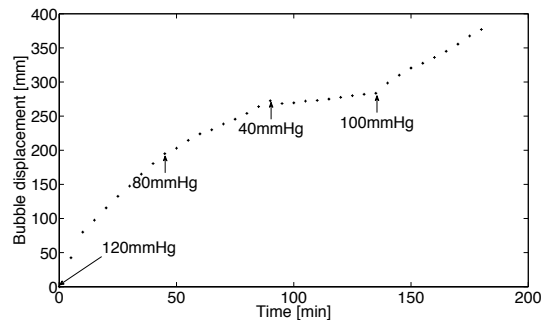


Figure 11: Typical displacement trace of bubble in flux measurement graduated tube. In this case, the bifurcation was placed under transmembrane pressures in the following order: 120mmHg, 80mmHg, 40mmHg and 100mmHg. Changes in pressure are indicated by arrows. The ‘sealing’ phenomenon previously reported (Baldwin et al., 1992) is observed in this trace within the first 15 min.

## References

- G.A. Ateshian and J.A. Weiss. Anisotropic hydraulic permeability under finite deformation. *Journal of biomechanical engineering*, 132(11):111004, 2010.
- G.A. Ateshian, W.H. Warden, J.J. Kim, R.P. Grelsamer, and V.C. Mow. Finite deformation biphasic material properties of bovine articular cartilage from confined compression experiments. *Journal of biomechanics*, 30(11):1157–1164, 1997.
- JR Baker. Principles of biological microtechnique. a study of fixation and dyeing. *Principles of biological microtechnique. A study of fixation and dyeing.*, 1958.
- A. L. Baldwin and L. M. Wilson. Endothelium increases medial hydraulic conductance of aorta, possibly by release of EDRF. *The American journal of physiology*, 264(1 Pt 2), 1993.
- A. L. Baldwin, L. M. Wilson, and B. R. Simon. Effect of pressure on aortic hydraulic conductance. *Arteriosclerosis, Thrombosis, and Vascular Biology*, 12(2):163–171, 1992.
- A. L. Baldwin, L. M. Wilson, I. Gradus-Pizlo, R. Wilensky, and K. March. Effect of atherosclerosis on transmural convection and arterial ultrastructure. *Arteriosclerosis, Thrombosis, and Vascular Biology*, 17(12):3365–3375, 1997.
- L. M. Cancel and J. M. Tarbell. The role of apoptosis in LDL transport through cultured endothelial cell monolayers. *Atherosclerosis*, 208(2):335–341, 2010.
- L. M. Cancel and J. M. Tarbell. The role of mitosis in LDL transport through cultured endothelial cell monolayers. *American Journal of Physiology - Heart and Circulatory Physiology*, 300(3):H769–H776, 2011.

- 1  
2 CD Cantwell, D Moxey, A Comerford, A Bolis, G Rocco, G Mengaldo, D De Grazia, S Yakovlev, J-E Lombard,  
3 D Ekelschot, et al. Nektar++: An open-source spectral/hp element framework. *Computer Physics Communica-*  
4 *tions*, 192:205–219, 2015.
- 5  
6 J. M. Clark and S. Glagov. Transmural organization of the arterial media. the lamellar unit revisited. *Arterioscle-*  
7 *rosis, Thrombosis, and Vascular Biology*, 5(1):19–34, 1985.
- 8  
9 A. Comerford, K. Y. Chooi, M. Nowak, P. D. Weinberg, and S. J. Sherwin. A combined numerical and experi-  
10 mental framework for determining permeability properties of the arterial media. *Biomechanics and modeling in*  
11 *mechanobiology*, 14(2):297–313, 2015.
- 12  
13 C. J. Creel, M. A. Lovich, and E. R. Edelman. Arterial paclitaxel distribution and deposition. *Circulation research*,  
14 86(8):879–884, 2000.
- 15  
16 M. Dabagh, P. Jalali, and Y. T. Konttinen. The study of wall deformation and flow distribution with transmural  
17 pressure by three-dimensional model of thoracic aorta wall. *Medical engineering & physics*, 31(7):816–824, 2009a.
- 18  
19 M Dabagh, P Jalali, and J M. Tarbell. The transport of LDL across the deformable arterial wall: the effect of  
20 endothelial cell turnover and intimal deformation under hypertension. *American journal of physiology. Heart and*  
21 *circulatory physiology*, 297(3):H983–H996, 2009b.
- 22  
23 C.R. Ethier. Flow through mixed fibrous porous materials. *AIChE journal*, 37(8):1227–1236, 1991.
- 24  
25 B A. Forster and P D. Weinberg. Changes with age in the influence of endogenous nitric oxide on transport  
26 properties of the rabbit aortic wall near branches. *Arteriosclerosis, Thrombosis, and Vascular Biology*, 17(7):  
27 1361–1368, 1997.
- 28  
29 D. L. Fry. *Response of the arterial wall to certain physical factors*, page 100. Associated Scientific Publishers, 52  
30 Vanderbilt Avenue, New York, N.Y, 1973.
- 31  
32 YC Fung and SS Sobin. The retained elasticity of elastin under fixation agents. *Journal of biomechanical engineering*,  
33 103(2):121–122, 1981.
- 34  
35 M.H. Holmes and V.C. Mow. The nonlinear characteristics of soft gels and hydrated connective tissues in ultrafil-  
36 tration. *Journal of biomechanics*, 23(11):1145–1156, 1990.
- 37  
38 G A. Holzapfel, T C. Gasser, and R W. Ogden. A new constitutive framework for arterial wall mechanics and a  
39 comparative study of material models. *Journal of Elasticity*, 61(1):1–48, 2000.
- 40  
41 G. A. Holzapfel, T. C. Gasser, and M. Stadler. A structural model for the viscoelastic behavior of arterial walls:  
42 Continuum formulation and finite element analysis. *European Journal of Mechanics - A/Solids*, pages 441–463,  
43 2002.
- 44  
45 G.A. Holzapfel and R.W. Ogden. Constitutive modelling of arteries. *Proceedings of the Royal Society of London A:*  
46 *Mathematical, Physical and Engineering Sciences*, 466(2118):1551–1597, 2010.
- 47  
48 Z. J. Huang and J. M. Tarbell. Numerical simulation of mass transfer in porous media of blood vessel walls.  
49 *American Journal of Physiology - Heart and Circulatory Physiology*, 273(1):H464–H477, 1997.
- 50  
51 CM Hurvich and C-L Tsai. Regression and time series model selection in small samples. *Biometrika*, 76(2):297–307,  
52 1989.
- 53  
54 C-W Hwang, D Wu, and E R. Edelman. Physiological transport forces govern drug distribution for Stent-Based  
55 delivery. *Circulation*, 104(5):600–605, 2001.
- 56  
57 M. Johnson and J. M. Tarbell. A biphasic, anisotropic model of the aortic wall. *Journal of biomechanical engineering*,  
58 123(1):52–57, 2001.
- 59  
60 W-S Kim and J M. Tarbell. Macromolecular transport through the deformable porous media of an artery wall.  
*Journal of Biomechanical Engineering*, 116(2):156+, 1994.
- M. Klanchar and J. M. Tarbell. Modeling water flow through arterial tissue. *Bulletin of mathematical biology*, 49  
(6):651–669, 1987.



- 1  
2 A.D. Levin, N. Vukmirovic, C-W. Hwang, and E.R. Edelman. Specific binding to intracellular proteins determines  
3 arterial transport properties for rapamycin and paclitaxel. *Proceedings of the National Academy of Sciences of*  
4 *the United States of America*, 101(25):9463–9467, 2004.
- 5  
6 S A Maas, B J Ellis, G A Ateshian, and J A Weiss. Febio: finite elements for biomechanics. *Journal of biomechanical*  
7 *engineering*, 134(1):011005, 2012.
- 8  
9 JRA Mitchell and CJ Schwartz. *Arterial disease*. Blackwell Scientific Publications, 1965.
- 10  
11 V. C. Mow, S. C. Kuei, W. M. Lai, and C. G. Armstrong. Biphasic creep and stress relaxation of articular cartilage  
12 in compression: Theory and experiments. *Journal of biomechanical engineering*, 102(1):73–84, 1980.
- 13  
14 J Schindelin, I Arganda-Carreras, E Frise, V Kaynig, M Longair, T Pietzsch, S Preibisch, C Rueden, S Saalfeld,  
15 B Schmid, J-Y Tinevez, D J. White, V Hartenstein, K Eliceiri, P Tomancak, and A Cardona. Fiji: an open-source  
16 platform for biological-image analysis. *Nat Meth*, 9(7):676–682, 2012.
- 17  
18 C M Shanahan, D L Connolly, K L Tyson, N RB Cary, J K Osbourn, P Agre, and P L Weissberg. Aquaporin-1  
19 is expressed by vascular smooth muscle cells and mediates rapid water transport across vascular cell membranes.  
20 *Journal of vascular research*, 36(5):353–362, 1999.
- 21  
22 Y Shou, K-M Jan, and D S. Rumschitzki. Transport in rat vessel walls. i. hydraulic conductivities of the aorta,  
23 pulmonary artery, and inferior vena cava with intact and denuded endothelia. *American Journal of Physiology -*  
24 *Heart and Circulatory Physiology*, 291(6):H2758–H2771, 2006.
- 25  
26 B. R. Simon, M. V. Kaufmann, M. A. McAfee, A. L. Baldwin, and L. M. Wilson. Identification and determination  
27 of material properties for porohyperelastic analysis of large arteries. *Journal of biomechanical engineering*, 120  
28 (2):188–194, April 1998.
- 29  
30 A.J.M. Spencer. *Continuum Mechanics*. Longman mathematical texts. Longman Scientific & Technical, 1980.
- 31  
32 A. Tedgui and M. J. Lever. Filtration through damaged and undamaged rabbit thoracic aorta. *American Journal*  
33 *of Physiology - Heart and Circulatory Physiology*, 247(5):H784–H791, 1984.
- 34  
35 A. Tedgui and M. J. Lever. The interaction of convection and diffusion in the transport of 131I-albumin within the  
36 media of the rabbit thoracic aorta. *Circulation research*, 57(6):856–863, 1985.
- 37  
38 ME Todd, CG Laye, and DN Osborne. The dimensional characteristics of smooth muscle in rat blood vessels. a  
39 computer-assisted analysis. *Circulation research*, 53(3):319–331, 1983.
- 40  
41 D. M. Wang and J. M. Tarbell. Modeling interstitial flow in an artery wall allows estimation of wall shear stress  
42 on smooth muscle cells. *Journal of biomechanical engineering*, 117(3):358–363, 1995.
- 43  
44 P. D. Weinberg, S. L. Carney, C. P. Winlove, and K. H. Parker. The contributions of glycosaminoglycans, collagen  
45 and other interstitial components to the hydraulic resistivity of porcine aortic wall. *Connect Tissue Res*, 36(4):  
46 297–308, 1997.
- 47  
48 J. A. Weiss and B. J. Maakestad. Permeability of human medial collateral ligament in compression transverse to  
49 the collagen fiber direction. *Journal of biomechanics*, 39(2):276–283, 2006.
- 50  
51  
52  
53  
54  
55  
56  
57  
58  
59  
60